Beyond reduction cocatalysts: critical role of metal cocatalysts in photocatalytic oxidation of methane with water

Hikaru Saito[1], Hiromasa Sato[1], Taisuke Higashi[1], Toshiki Sugimoto*[,1,2]

[1]Department of Materials Molecular Science, Institute for Molecular Science, Okazaki, Aichi 444-8585, Japan

[2]Precursory Research for Embryonic Science and Technology (PRESTO), Japan Science and Technology Agency (JST), Chiyoda, Tokyo 102-0076, Japan

*Corresponding author (E-mail: toshiki-sugimoto@ims.ac.jp)

Abstract

Environmentally sustainable and selective conversion of methane to valuable chemicals under ambient conditions is pivotal for the development of next-generation photocatalytic technology. However, due to the lack of microscopic knowledge about non-thermal methane conversion, controlling and modulating photocatalytic oxidation processes driven by photogenerated holes remain a challenge. Here, we report novel function of metal cocatalysts to accept photogenerated holes and dominate the oxidation selectivity of methane, which is clearly beyond the conventional concept in photocatalysis that the metal cocatalysts loaded on the surfaces of semiconductor photocatalysts mostly capture photogenerated electrons and dominate reduction reactions exclusively. The novel photocatalytic role of metal cocatalysts was verified by *operando* molecular spectroscopy combined with real-time mass spectrometry for metal-loaded Ga_2O_3 model photocatalysts under methane gas and water vapor at ambient temperature and pressure. Our concept of metal cocatalysts that work as active sites for both photocatalytic oxidation and reduction provides a new understanding of photocatalysis and a solid basis for controlling the non-thermal redox reactions by metal-cocatalyst engineering.

Introduction

Conversion of methane to desirable chemicals is a key area of research in catalytic chemistry because methane is a ubiquitous hydrocarbon resource as well as a greenhouse gas. However, the chemical utilization of methane, in most cases, is energy intensive because of the high stability of methane originating from the non-polar and robust C–H covalent bond[1]. The conventional steam reforming of methane requires harsh conditions (~1250 K and ~3 MPa)[1] for producing syngas (carbon monoxide and hydrogen). In contrast, heterogeneous photocatalysis as a non-thermal catalytic process offers great advantages such as allowing methane oxidation to be carried out under ambient conditions by utilizing photon energy[2–7]. The photocatalytic conversion of methane with a ubiquitous and clean oxidant of water has potential to develop into an on-site and on-demand chemical technology for the green utilization of methane in an environmentally benign and sustainable way.

To expand the scope of practical application of photocatalytic methane conversion, rational design of photocatalysts is essential for achieving high photocatalytic activity and selectivity toward a target chemical. To date, numerous studies have been devoted to the fabrication of photocatalysts that exhibit high visible-light sensitivity[8–10] and quantum efficiency[11–13] based on their bulk properties such as the band gap energy and the lifetime of photogenerated carriers (e^- and h^+). In photocatalysis, the oxidation reaction is known to be triggered by the photogenerated holes at the catalyst surfaces[4]. To develop innovative next-generation photocatalytic technologies, control of the surface oxidation reactions is of particular importance to produce valuable chemicals through partial oxidation reactions. However, controlling the non-thermal methane oxidation remains a challenge due to the lack of microscopic understanding of the behavior of photogenerated holes at the surface and the resultant hole-driven oxidation kinetics, thus limiting the fabrication of an innovative photocatalyst for methane conversion. It is therefore necessary to clarify the key factors associated with the surface oxidation reactions.

Herein, we report the combinational experimental approach of the real-time mass spectrometric analysis of the photocatalytic reaction products with *operando* molecular spectroscopy of photocatalyst surfaces to systematically demonstrate that metal cocatalysts can play a crucial role as hole acceptor sites and have significant impacts on the hole-driven oxidation reactions of methane. The reaction kinetics and selectivity of photocatalytic methane oxidation vary significantly depending on the metal cocatalysts (Pt and Pd) supported on the surface of the β-Ga_2O_3 photocatalyst. Our systematic experimental results provide a new paradigm for the role of the metal cocatalyst in photocatalysis, which is beyond the conventional assumption that the metal cocatalyst accumulates mostly photogenerated electrons and induces reduction reactions exclusively[14–18].

Results and discussion

Influence of the partial pressure of methane on photocatalytic performance. In the present study, we chose β-Ga_2O_3, a well-known d^{10} photocatalyst[15], as a model of the metal oxide photocatalyst because of its robustness and enough redox potential for oxidation of methane and water[19, 20]. Following the preparation of metallic platinum- and palladium-loaded β-Ga_2O_3 (Pt/Ga_2O_3 and Pd/Ga_2O_3) photocatalysts (see Methods and Supplementary Section 5 for details), the photocatalytic activities of these systems were investigated at several methane gas pressures (P_{CH4}) under wet conditions, where the water vapor pressure was fixed at P_{H2O} = 2 kPa. At the typical reaction temperature of 323 K, a P_{H2O} value of 2 kPa corresponds to a relative humidity of ~17%, wherein the photocatalyst surfaces are covered with approximately a single layer of adsorbed water molecules[21], as described in Supplementary Section 1. We confirmed that the quantity of gaseous products increased almost linearly upon increasing the UV irradiation time (Fig. S3 in Supplementary Information), thereby indicating that the photocatalytic reactions proceeded under almost steady-state conditions.

Loading the Pt cocatalyst greatly enhanced both photocatalytic oxidation and reduction activities of bare Ga_2O_3 (Fig. S4a) with the reduction and oxidation reactions almost balanced (Fig. S5), while the selectivity of Pt/Ga_2O_3 was almost unchanged in comparison to that of bare Ga_2O_3 (Fig. S4b). The major products, namely H_2 and CO_2, were attributed to the total oxidation of methane in the presence of water ($CH_4 + 2H_2O \rightarrow CO_2 + 4H_2$), and a small amount of CO (i.e., an intermediate for CO_2 formation)[22] was also formed simultaneously. As a side reaction, O_2 formation was also observed, particularly at low values of P_{CH4} (Fig. S5), indicating the occurrence of water splitting ($H_2O \rightarrow H_2 + 1/2O_2$). In addition, the partial oxidation of methane to ethane ($2CH_4 \rightarrow C_2H_6 + H_2$) proceeded simultaneously via the coupling of methyl radicals[19, 20]. Although water itself is not involved in the equation of methane coupling ($2CH_4 \rightarrow C_2H_6 + H_2$), the presence of the adsorbed water layer enhanced ethane formation (Fig. S6).

Fig. 1a shows the formation rates of CO_2 (r_{CO2}) and ethane (r_{C2H6}) over the Pt/Ga_2O_3 photocatalyst at various values of P_{CH4}. The formation rates of these gaseous products changed with an increase in P_{CH4}; r_{CO2} increased steeply to 30 kPa and gradually reached a plateau at P_{CH4} values > 30 kPa while r_{C2H6} increased sigmoidally as featured in the low P_{CH4} region, and overall, these formation rates were saturated up to ~100 kPa (1 atm). These results indicate that the Pt/Ga_2O_3 photocatalyst displays maximum performance under ambient conditions.

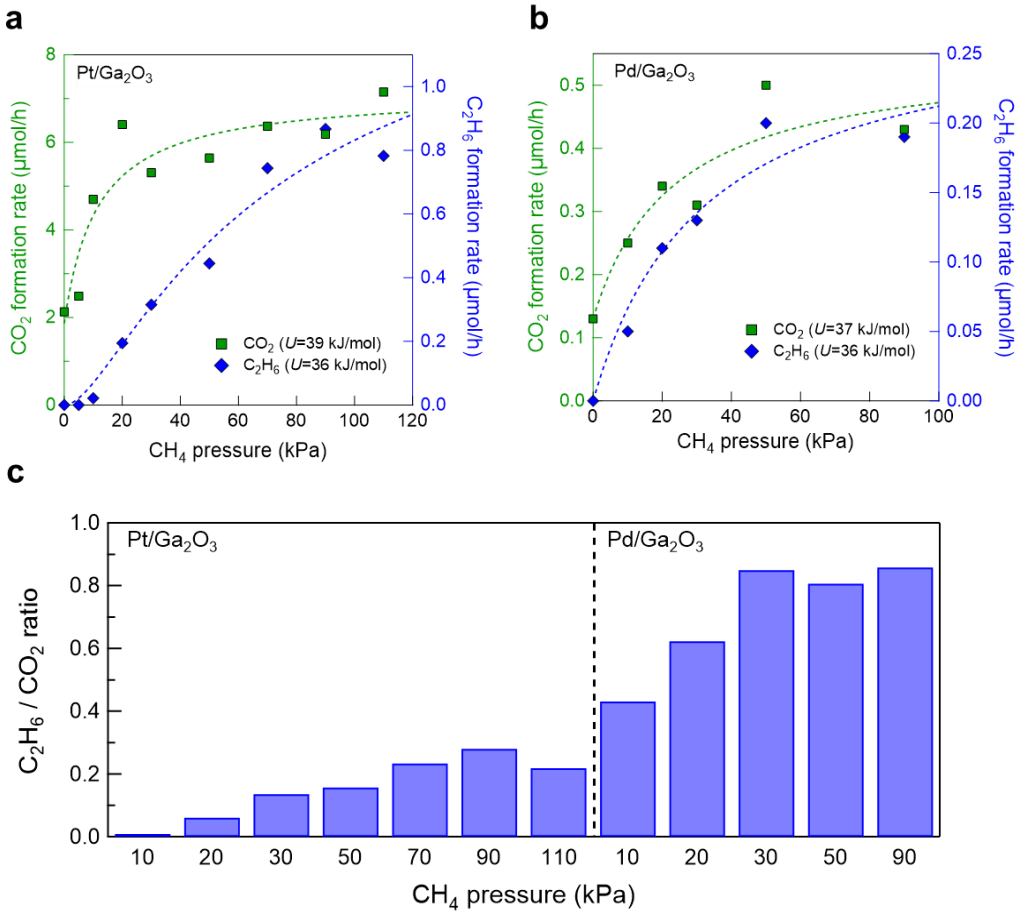

Fig. 1 | Photocatalytic activities and selectivities at various values of P_{CH4}. a, b, Formation rates of CO_2 and C_2H_6 over Pt/Ga_2O_3 (**a**) and Pd/Ga_2O_3 (**b**). The partial pressure of water vapor was fixed at 2 kPa. The dashed lines were drawn on the basis of kinetic analyses using the stabilization energy (U) of the first adsorbed methane species (X_1) as a fitting parameter (see also Supplementary Section 3). **c**, The C_2H_6 to CO_2 ratios calculated from the number of carbon atoms of converted methane ($2r_{C2H6}/r_{CO2}$).

The observed P_{CH4} profile of r_{CO2} was not specific to Pt/Ga_2O_3. As shown in Fig. 1b, a similar behavior was obtained in the case of Pd/Ga_2O_3, although CO was not detected as a gaseous product for this photocatalyst (Fig. S5). In contrast, the P_{CH4}-dependence of r_{C2H6} over Pd/Ga_2O_3 was different from that observed for Pt/Ga_2O_3; r_{C2H6} also increased with elevated values of P_{CH4} similar to r_{CO2}. Importantly, the loading of the Pd cocatalyst markedly changed the selectivity of bare Ga_2O_3 while their photocatalytic activities were comparable (Fig. S4); the Pd/Ga_2O_3 photocatalyst exhibited a higher selectivity for ethane than bare Ga_2O_3 and Pt/Ga_2O_3 (Fig. 1c). This feature of the Pd cocatalyst is in stark contrast to that of the Pt cocatalyst that enhances the photocatalytic activity but has little influence on the oxidation selectivity of bare Ga_2O_3 (Fig. S4). Moreover, the trend of the oxidation selectivity did not vary with the loading amount of the metal cocatalysts (Fig. S7). These results suggest that the oxidation selectivity is an element-specific feature of the metal cocatalyst. Thus, the metal cocatalysts play a decisive role in determining the selectivity of hole-driven oxidation of methane, which is clearly beyond the basic

understanding in the field of photocatalysis that the metallic cocatalysts mostly capture photogenerated electrons and affect reduction reactions exclusively[17].

Detailed kinetic analysis for the P_{CH4}-dependent oxidation toward CO_2 and C_2H_6. The observed P_{CH4} profiles of r_{CO2} and r_{C2H6} provide microscopic insight into the kinetics of the methane oxidation reaction. In the conventional thermal catalytic transformation of methane, the first C–H activation process is generally the rate-determining step[23, 24], and so the methane conversion rate increases linearly with P_{CH4}. The peculiar non-linear P_{CH4}-dependence observed in the photocatalytic methane conversion (Fig. 1) therefore indicates that the rate-determining step is different from this initial C–H activation step. Furthermore, the P_{CH4} profiles for Pt/Ga_2O_3 and Pd/Ga_2O_3 represent different features in the partial oxidation process, suggesting mechanistic differences in the formation of ethane depending on the metal cocatalysts.

As shown in Fig. 2a, the methane oxidation process on the photocatalyst surface can be roughly divided into three steps: (i) The adsorption and desorption of methane, (ii) sequential reactions of the surface intermediate species, and (iii) desorption of the final products from the surface. The total oxidation to CO_2 proceeds through an eight-hole process[25, 26] and a detailed reaction pathway from adsorbed methane to CO_2 via several intermediate species is shown in Fig. 2b while the partial oxidation to ethane proceeds through a two-hole process and is simply regarded as a coupling of dissociatively adsorbed methane species, i.e., methyl radicals[27] (Fig. 2c). Based on the detailed kinetic analyses provided in Supplementary Section 3, the observed P_{CH4} profiles of r_{CO2} and r_{C2H6} for the Pt/Ga_2O_3 photocatalyst under steady-state reaction conditions could be simply described as the first- and second-order reactions of the initially adsorbed intermediate X_1 as $r_{CO_2} \propto \theta_{X_1}$ and $r_{C_2H_6} \propto \theta_{X_1}{}^2$, respectively, where θ_{X1} is the coverage of X_1 characterized by the Langmuir adsorption isotherm-like P_{CH4}-dependence as follows:

$$\theta_{X_1} = \frac{P_{CH_4}}{P_{CH_4} + K^{-1}} \qquad (1)$$

where K denotes the equilibrium constant for the adsorption and desorption of methane and is defined as $K \equiv (k_{ad}/k_{de}) \propto \exp(U/k_B T_s)$ as described in Supplementary Section 3. Also, k_B and T_s are the Boltzmann constant and the photocatalyst surface temperature, respectively, while U is the stabilization energy of the X_1 intermediate species relative to the methane molecule in the gas phase. As shown in Fig. S9, the critical P_{CH4} value at which θ_{X1} increases substantially is determined by U. In the case of the Pt/Ga_2O_3 photocatalyst, the U values were estimated to be 39 and 36 kJ/mol for CO_2 and C_2H_6 (Fig. 1a and Table S4), respectively, which are approximately three times larger than the physisorption energy of methane molecules (i.e., ~13 kJ/mol, Table S2). Based on the comparable U values of the order of ~40

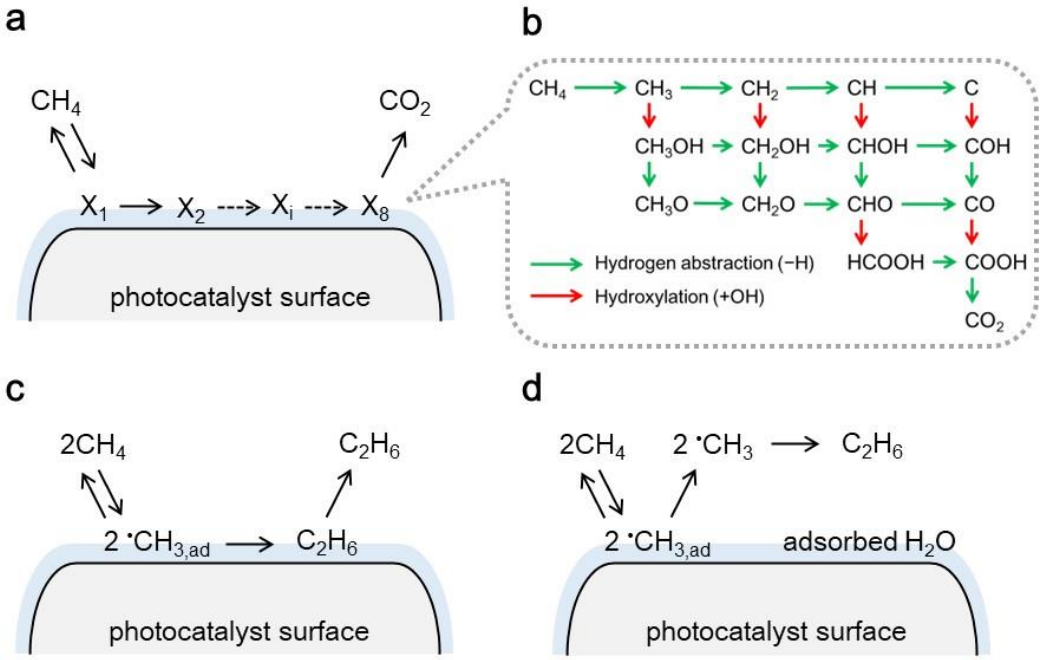

Fig. 2 | Schematic diagrams of the total and partial oxidation processes. a, The total oxidation process on the photocatalyst surface. **b**, Possible reaction pathway and intermediates in the oxidation of methane to produce CO_2[25, 26]. **c**, **d**, The partial oxidation to ethane through the coupling of methyl radicals on the photocatalyst surface (**c**) and in the gas phase (**d**).

kJ/mol for the CO_2 and C_2H_6 formation, we can reasonably assume that the initially adsorbed reaction intermediate X_1 is dissociatively chemisorbed methane, i.e., methyl radicals (X_1 = $^{\bullet}CH_3$). Namely, methane molecules adsorb on the photocatalyst surface accompanied by the C–H bond cleavage.

A pronounced difference in the oxidation behavior was observed for the Pd/Ga_2O_3 photocatalyst. While the P_{CH4}-dependence of r_{CO2} for Pd/Ga_2O_3 (Fig. 1b) was described well by the first-order surface reaction scheme analogous to Pt/Ga_2O_3, the behavior distinct from the second-order reaction scheme was observed for ethane formation (Fig. 1b); the P_{CH4}-dependence of r_{C2H6} for Pd/Ga_2O_3 was also described well by the first-order reaction scheme. Therefore, in stark contrast to Pt/Ga_2O_3, the reaction scheme of ethane formation over the Pd/Ga_2O_3 photocatalyst could not be described as a simple surface coupling of adsorbed $^{\bullet}CH_3$. As discussed in Supplementary Section 3 for details, the apparent first-order behavior for Pd/Ga_2O_3 is a manifestation of the gas-phase coupling of the desorbed free $^{\bullet}CH_3$ intermediates (Fig. 2d) or coupling of the adsorbed $^{\bullet}CH_3$ with the free $^{\bullet}CH_3$ species (Fig. S8d). In the former reaction scheme (Fig. 2d), the desorption of the adsorbed $^{\bullet}CH_3$ intermediates from the photocatalyst surface to the gas phase is characterized by the first-order process of θ_{X1}, and r_{C2H6} can be described by the square of the concentration of the free $^{\bullet}CH_3$ species in the gas phase as $r_{C_2H_6} \propto \left[\bullet CH_{3,gas}\right]^2$. Under the steady-state reaction conditions, the flux of the first-order desorption of the adsorbed $^{\bullet}CH_3$ species is balanced with that of the second-order coupling reaction of the free $^{\bullet}CH_3$ species in the gas phase, resulting in a

proportional relationship between θ_{X1} and $[^{\bullet}CH_{3,gas}]^2$ (see Eq. S18 in Supplementary Section 3). This proportional relationship between θ_{X1} and r_{C2H6} is also satisfied in the latter reaction scheme: the coupling of the adsorbed $^{\bullet}CH_3$ with the free $^{\bullet}CH_3$ species (Fig. S8d). Therefore, the P_{CH4} profile of r_{C2H6} for Pd/Ga_2O_3 (Fig. 1b) described by the first-order Langmuir adsorption isotherm-like behavior as $r_{C_2H_6} \propto \theta_{X_1}$ strongly indicates that the free $^{\bullet}CH_3$ species released to the gas phase are involved in the ethane formation processes for the Pd/Ga_2O_3 photocatalyst in contrast to the Pt/Ga_2O_3 photocatalyst (Fig. 2c).

It is worth noting that the U values calculated from the kinetic analyses for the CO_2 and C_2H_6 formation were energetically comparable as also presented in Table S4, suggesting that the microscopic origin of the initial C–H activated surface intermediate ($^{\bullet}CH_3$) is common to both the total and partial oxidation processes[20]. Nevertheless, the ratio of C_2H_6 production to CO_2 production (Fig. 1c) as well as the surface and gas-phase reaction pathways for the partial oxidation processes was dramatically different depending on the metal cocatalysts. Our experimental results therefore demonstrate that metal cocatalysts have a fundamental influence on the oxidation kinetics/dynamics and photocatalytic selectivity, which is clearly beyond the conventional understanding of the roles of metal cocatalysts. Although metal cocatalysts such as Pt and Pd have been believed to promote separation of the photogenerated charges (e^- and h^+) by predominantly capturing the photogenerated electrons and inducing reduction reactions such as H_2 evolution ($2H^+ + 2e^- \rightarrow H_2$)[17, 18], our results show that the hole-driven oxidation reactions, particularly the partial oxidation, was also modulated depending on the metallic cocatalysts.

Spectroscopic observation of the reaction intermediates. To obtain further evidence on the impact of the metal cocatalysts on the photocatalytic oxidation reactions, we performed *operando* diffuse reflectance infrared Fourier transform (DRIFT) spectroscopy. The *operando* DRIFT spectra for hydrocarbon and CO intermediate species (Figs. 3, S11, and S12) recorded under the reaction condition demonstrate the differences in the oxidation kinetics/dynamics of these intermediate species for the Pt/Ga_2O_3 and Pd/Ga_2O_3 photocatalysts. In the C–H stretching spectra for Pt/Ga_2O_3 (Fig. 3a), three absorption bands were observed at 2975, 2907, and 2818 cm^{-1}, which are attributed to the antisymmetric and symmetric stretching vibrations of the adsorbed methane species[28, 29] and the C–H symmetric stretching vibration of the methoxy groups[30, 31]. Since methane molecules cannot adsorb on the photocatalyst surfaces under ambient conditions without UV irradiation due to the extremely low adsorption energy (i.e., ~13 kJ/mol, Table S2), the observed hydrocarbon species were derived from the intermediate species generated through the photocatalytic processes. With additional experiments (Fig. S13) and discussion described in Supplementary Section 4, we also concluded that the observed surface hydrocarbon and CO species were active intermediate species rather than inert spectators.

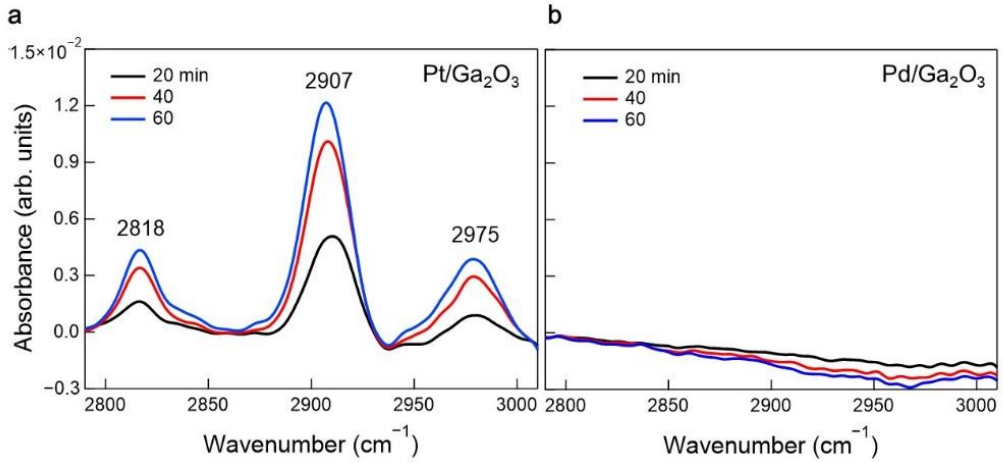

Fig. 3 | *Operando* DRIFT spectra in the C–H stretching region. a, **b**, Changes in the *operando* DRIFT spectra of the hydrocarbons adsorbed on Pt/Ga_2O_3 (**a**) and Pd/Ga_2O_3 (**b**) with variation in the UV irradiation time. All spectra were measured at methane and water partial pressures of 30 and 2 kPa, respectively.

In contrast to Pt/Ga_2O_3, no absorption bands derived from the adsorbed hydrocarbon intermediates were detected for Pd/Ga_2O_3 (Fig. 3b). Because methane conversion to CO_2 and C_2H_6 proceeds via the hydrocarbon intermediates such as CH_3 species (Fig. 2), the apparent absence of C–H stretching bands is ascribed to a low population of the hydrocarbon intermediates on the Pd/Ga_2O_3 surface due to a considerable difference in the oxidation dynamics; it is estimated from the difference in IR absorbance (Fig. 3) and r_{CO2} (Fig. 1) that the consumption rate of the adsorbed hydrocarbon intermediates over the Pd/Ga_2O_3 photocatalyst is at least one order of magnitude faster than that over the Pt/Ga_2O_3 photocatalyst. Moreover, the absence of the C–H peaks for Pd/Ga_2O_3 is in accordance with the reaction schemes of ethane formation through the gas-phase coupling of the methyl radical intermediates (Fig. 2d). Thus, the C–H stretching spectra shown in Fig. 3 corroborate the difference in the oxidation dynamics of the hydrocarbon intermediates between the Pt and Pd cocatalysts.

The difference in the oxidation dynamics between the Pt/Ga_2O_3 and Pd/Ga_2O_3 photocatalysts was also clearly observed in the spectra for the adsorbed CO intermediate species in the total oxidation process (Fig. S12). Note that the desorption of the adsorbed CO intermediate to the gas phase as a gaseous product was verified only for the Pt/Ga_2O_3 photocatalyst (Fig. S5). These results suggest that the behaviors of the CO intermediates, i.e., desorption and further surface oxidation, are modulated drastically depending on the metal cocatalysts; CO oxidation to CO_2 is much preferable to CO desorption for Pd/Ga_2O_3 whereas CO oxidation competes with CO desorption for Pt/Ga_2O_3.

The impact of the metal cocatalysts on the intermediate dynamics was further supported by *operando* DRIFT spectroscopy for bare Ga_2O_3. As shown in Fig. S14, absorption bands of both C–O and C–H stretching modes were not observed for this sample. Because bare Ga_2O_3 exhibited a comparable

activity to Pd/Ga_2O_3 and higher CO_2 selectivity than Pd/Ga_2O_3 (Fig. S4), the absence of C–O stretching bands indicates that the CO intermediates are unstable on the Ga_2O_3 surface while the metallic cocatalysts stabilize the CO intermediates and prolong their lifetime, i.e., residence time, on their surfaces. The observation for the bare Ga_2O_3 photocatalyst also strongly suggests that the metal cocatalysts are directly involved in the methane oxidation processes (Fig. 2b) driven by photogenerated holes.

Manifestation of hole accumulation at the metallic cocatalyst sites. Further differences in the hole-driven oxidation behaviors were verified explicitly in terms of the oxidation states of the Pt and Pd cocatalysts. The oxidation state and coordination environment of the surface metal atoms are well known to be sensitively probed by stretching frequencies of CO adsorbates[32, 33]. In our experiments, the adsorbed CO species are generated as an intermediate (Figs. 2b, 4a, and S12). Therefore, we can evaluate the oxidation states of the metal cocatalysts under the employed reaction conditions based on the *operando* DRIFT spectra of the adsorbed CO intermediate. For this *operando* observation, we used the $H_2{}^{18}O$ water isotope to trace water-derived oxidation intermediate species. In this case, the wavenumbers of the C–^{18}O

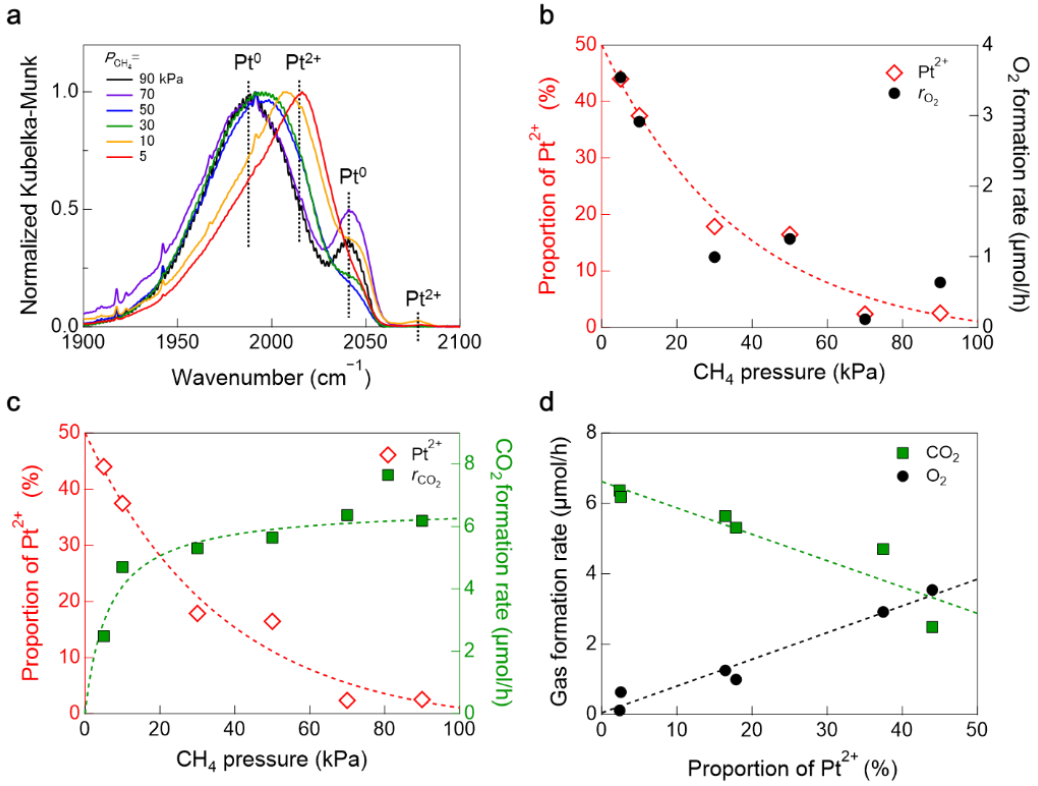

Fig. 4 | Relationship between the oxidation state of Pt and evolution of O_2 and CO_2. a, *Operando* DRIFT spectra of $C^{18}O$ adsorbed on the Pt/Ga_2O_3 surface at different values of P_{CH4} under steady-state reaction conditions. The spectra were measured at a $H_2{}^{18}O$ partial pressure of 2 kPa. **b**, **c** Variation in the Pt^{2+} and formation rates of O_2 and CO_2 at various methane partial pressures. The proportion of Pt^{2+} was calculated form the peak deconvolution of the $C^{18}O$ absorption bands (Supplementary Fig. S12e) **d**, Linear relationship between the proportion of Pt^{2+} and formation rates of O_2 and CO_2.

stretching modes are red-shifted by ~50 cm^{-1} compared to the non-labelled $C^{16}O$ molecule[34]. Note that the use of the labelled water had no appreciable kinetic isotope effect as reported in our recent study[20], indicating that the isotope labelling of oxygen does not affect the reaction kinetics/dynamics.

Fig. 4a shows the *operando* DRIFT spectra of the $C^{18}O$ intermediates adsorbed on Pt/Ga_2O_3, wherein the broad asymmetric $C–^{18}O$ stretching band includes two components at ~2015 and ~1990 cm^{-1}; these peaks are attributed to $C^{18}O$ molecules adsorbed on coordinatively unsaturated Pt^{2+} and Pt^0 sites, respectively[32, 33]. In contrast, the absorption bands at ~2080 and ~2045 cm^{-1} are attributed to the $C^{18}O$ molecules adsorbed on coordinatively saturated Pt^{2+} and Pt^0 terrace sites[32, 33]. In the case of Pd/Ga_2O_3, a broad absorption band was observed at ~1880 cm^{-1} (Fig. S12d), which is attributed to bridging $C^{18}O$ species at low coverage, or to the $C^{18}O$ molecules adsorbed on the three-fold hollow sites of metallic Pd (i.e., Pd^0)[35].

As shown in Fig. 4a, the spectral shape of the adsorbed $C^{18}O$ intermediate under steady-state reaction conditions markedly changed with P_{CH4} for the Pt/Ga_2O_3 system. More specifically, the peak at ~2015 cm^{-1} gradually red-shifted toward that at ~1990 cm^{-1}. This result demonstrates that the stable oxidation state of the Pt cocatalyst changed gradually depending on P_{CH4}. Although the oxidation state of Pt on the Ga_2O_3 surface was metallic (Pt^0) prior to UV irradiation (see Methods and Fig. S16), the Pt cocatalyst was partially oxidized toward PtO during the reaction at low P_{CH4} whereas metallic Pt was dominant at high P_{CH4} values. In contrast to Pt/Ga_2O_3, such a pronounced P_{CH4}-dependence was not observed for the Pd/Ga_2O_3 system (Fig. S12d), thereby indicating that the metallic state is stably maintained for the Pd cocatalyst irrespective of P_{CH4}.

In good correspondence with the difference in the oxidation behaviors of these metal cocatalysts, the formation rate of O_2 (r_{O2}) simultaneously produced via water splitting also changed dramatically depending on the metal cocatalysts; whereas Pd/Ga_2O_3 exhibited no activity for the O_2 evolution reaction, Pt/Ga_2O_3 was active for water splitting at low P_{CH4} (Fig. S5). Importantly, the P_{CH4} profile of r_{O2} is well correlated with the Pt oxidation (Fig. 4b); the proportion of Pt^{2+} decreased with elevated values of P_{CH4}, in line with the decrease in r_{O2}. The positive linear relationship between the proportion of Pt^{2+} and r_{O2} (Fig. 4d) demonstrates that the oxidation of metallic Pt is accompanied by water splitting; the photoactivation of the adsorbed water molecules proceeds on the Pt surface rather than on the Ga_2O_3 surface. Given that adsorbed water molecules are oxidized by photogenerated holes[20, 36–38], our results strongly indicate that the Pt cocatalyst accumulates the photogenerated holes and is involved in the photocatalytic oxidation reactions.

Then, it is reasonably anticipated that the photoactivated water species begin to preferentially react with methane molecules rather than water molecules themselves by increasing the P_{CH4} value. Such

behavior was observed as shown in Figs. 4b and 4c; the P_{CH4} profile of r_{O2} is inversely correlated with that of r_{CO2}. Because the photoactivated water species that induce the oxidation of Pt at low P_{CH4} were consumed for CO_2 formation, the metallic Pt state is maintained at the higher P_{CH4} (Fig. 4c). The negative linear relationship between the proportion of Pt^{2+} and r_{CO2} provides solid evidence that the hole-driven oxidation of methane and water proceeds on the Pt cocatalyst.

Although the Pd cocatalyst was not oxidized under the reaction conditions employed herein, the methane oxidation kinetics and selectivity were indeed modulated in comparison with those of Pt/Ga_2O_3 and bare Ga_2O_3 systems as discussed above. In addition, the observation of the CO intermediates adsorbed on the Pd cocatalyst also demonstrates that the total oxidation process (Fig. 2b) proceeds on the metallic Pd surface. Thereby the photogenerated holes accumulate also at the Pd cocatalyst and have the significant impact on the oxidation reaction occurring on the Pd/Ga_2O_3 surface. Since metallic Pd possesses a higher Fermi level than metallic Pt[17], the trapped holes at the metallic Pd cocatalysts are likely more stabilized and have less oxidation ability in comparison with those at the metallic Pt cocatalysts. Therefore, the energy level of trapped holes in these metal cocatalysts would be an important factor of oxidation selectivity in photocatalysis.

Before conclusion, it should be remarked that metallic cocatalysts (Pt, Pd, Rh, *etc.*) have generally been recognized as reduction cocatalysts that capture photogenerated electrons and promote reduction reactions such as H_2 evolution, while oxidation reactions are generally believed to be accelerated by non-metallic cocatalysts such as metal oxides (CoO_x, CuO_x, PdO_x, *etc.*)[14–18] as reported in various spectroscopic and theoretical studies[39–43]. Although the possibility of hole accumulation in the metallic cocatalyst was discussed in the previous DFT calculation[44] and surface molecular spectroscopy[45], these studies assumed that the hole-accumulated metal cocatalyst acts as just a recombination center of the photogenerated charges (e^- and h^+) and cannot promote well the photocatalytic reactions[44, 45]. In contrast to this previous assumption, our work demonstrates that the metallic cocatalyst not only enhances the photocatalytic activity for both oxidation and reduction but also modulates the oxidation selectivity and reaction kinetics/dynamics of methane and water (Figs. 1–4, S4, S5, and S12). The photogenerated holes and electrons are therefore likely to be separately trapped by different metal cocatalyst particles[46, 47] while avoiding recombination, and inducing the oxidation and reduction reactions, respectively.

Finally, we remark that our new concept of the metal cocatalyst also rationalizes well the previously reported incomprehensible results in the photocatalytic oxidation of organic molecules[48–51]. For instance, it has been recognized in the photocatalytic synthesis of diverse organic molecules that the selectivity of organic products significantly depends on the metal cocatalyst employed[49, 50]. Nevertheless, the metal cocatalysts have been assumed to be involved only in reduction reactions[49, 50]. Despite intensive research in the past, this contradictory interpretation has widely prevailed in the field of photocatalysis;

the functional role of the metallic cocatalyst in oxidation selectivity remains elusive. Beyond the classical picture of the metal cocatalyst in photocatalysis, our results suggest that the metal cocatalyst actively takes part in photocatalytic oxidation and modulates oxidation kinetics/dynamics.

Conclusion

In this study, we have demonstrated for the first time that metal cocatalysts play key roles as acceptor sites for photogenerated holes without accelerating charge recombination. Combining real-time mass spectrometry with *operando* molecular spectroscopy, we showed that the Pt-loaded photocatalyst predominantly promoted the total oxidation of methane toward CO_2 on its surface, while the Pd-loaded photocatalyst exhibited a higher selectivity for ethane formation through the gas-phase coupling of free methyl radicals. These results clearly indicate that the metal cocatalysts dominate the photocatalytic oxidation of methane with water and, hence, modulate the hole-driven oxidation dynamics and reaction pathways, which is in contrast to the traditional belief that metal cocatalysts are mostly the sites for the accumulation of photogenerated electrons and reduction reactions. The systematic and well-designed investigation of the photocatalytic oxidation of methane (i.e., the most inert and simplest organic compound) and water (i.e., one of the key molecules in photocatalysis) provides a new paradigm for the role of the metal cocatalysts and thus establishes a conceptual basis for controlling non-thermal oxidation reactions under ambient conditions.

Methods

Photocatalyst preparation. Commercial β-Ga_2O_3 (Kojundo Chemical Lab., purity >99.99%) was employed to prepare platinum- and palladium-loaded samples (Pt/Ga_2O_3 and Pd/Ga_2O_3) using an impregnation method. The loading amounts of Pt and Pd were 1 wt%. Initially, H_2PtCl_6•$6H_2O$ (Fujifilm Wako Chemicals, purity >99.9%) or $PdCl_2$ (Kishida Chemical, purity >99%) was dissolved in deionized water. The required amounts of Pt and Pd precursors were 26.6 and 16.8 mg, respectively, to prepare 1 g of Pt/Ga_2O_3 and Pd/Ga_2O_3. These aqueous solutions were added to a dispersion of Ga_2O_3 particles in deionized water. The resulting slurry was then heated at 368 K for 1.5 h using a magnetic stirrer-hotplate. After that, the solvent was evaporated completely, and the obtained powder was dried overnight in an oven at 373 K. Finally, calcination was carried out for 2 h at 673 K using a muffle furnace. The as-prepared Pt- and Pd-loaded Ga_2O_3 photocatalysts were further reduced in H_2 and subsequently used for the photocatalytic reaction and *operando* DRIFT spectroscopy without exposure to air, as described in detail below.

Evaluation of photocatalytic activity. The photocatalytic conversion of methane in the presence of water vapor was performed in a batch reactor. Our reaction chamber and gas-dosing lines are constructed with stainless-steel ConFlat flanges sealed by metal gaskets and were evacuated to ultra-high vacuum by a turbomolecular pump. Quadrupole mass spectrometer (QMS, QMG220; Pfeiffer Vacuum) operated under ultra-high vacuum conditions confirmed that there is no appreciable leakage of air. Moreover, high-purity gaseous samples were used in our experiments; ultrapure water ($H_2{}^{16}O$; Fujifilm Wako Chemicals) and $H_2{}^{18}O$ (Taiyo Nippon Sanso) were carefully degassed by freeze-pump-thaw cycling under ultra-high vacuum conditions and highly purified methane (Sumitomo Seika, purity >99.99%) was used as a gaseous reactant. Any contamination of oxygen impurities is therefore negligible. The as-prepared photocatalyst (~20 mg) was mounted on a stainless-steel chamber and reduced under H_2 (2 kPa) at 393 K for 3 min. These conditions are sufficient to reduce Pt and Pd oxide species[52, 53] and the presence of metallic Pt and Pd was verified by various techniques (see Supplementary Section 5 for details). After cooling the reduced photocatalyst to room temperature (296 K) and evacuating H_2 gas, methane and water were introduced into the reaction chamber without exposing the reduced samples to air. The partial pressure of methane (P_{CH4}) was varied in the range of 0–110 kPa, while that of water (P_{H2O}) was fixed at 2 kPa. Deep UV light emitted from an Hg-Xe lamp (UXM-500SX; Ushio) was irradiated through a 3 mm thick CaF_2 window. The intensity of the deep UV light was ~90 mW/cm^2, as measured using a UV meter (UVR-300; TOPCON). Under UV irradiation, the temperature of the photocatalyst immediately increased from 296 K (room temperature) to ~323 K at which coverage of adsorbed water is estimated to be about one monolayer at 2 kPa of water vapor (see Supplementary Section 1 for details). The gaseous products, including H_2, O_2, CO, CO_2, and C_2H_6, were quantified using a well-calibrated QMS. As described in Supplementary Section 6 for details, the fragmentation of ethane and other gas was taken into account for the quantification of the gaseous products such as CO and C_2H_6.

***Operando* DRIFT spectroscopy.** The surface-adsorbed species present under the reaction conditions employed in this study were observed using *operando* diffuse reflectance infrared Fourier transform (DRIFT) spectroscopy. The optical system was integrated with the reactor used in the activity tests, and the DRIFT spectra were recorded using an infrared spectrometer (FT/IR-6600; JASCO) equipped with a mercury–cadmium–telluride detector. The *operando* DRIFT spectra for the reduced Pt- and Pd-loaded Ga_2O_3 photocatalysts were measured at P_{CH4} and P_{H2O} values of 30 and 2 kPa under UV irradiation. In addition, the *operando* DRIFT spectra of the adsorbed CO were measured at various P_{CH4} values to evaluate the oxidation state of Pt. Since the spectral shape changed drastically during the initial state of the reaction, we employed the spectra collected after 60 min of the reaction to carry out peak analysis. The spectra of adsorbed CO were deconvoluted with three Gaussian functions, and the proportion of Pt^{2+}

was calculated based on the peak areas of the deconvoluted peaks. During the measurements, isotopically labelled $H_2{}^{18}O$ water was employed to exclude a possibility of a direct contribution of lattice ^{16}O species of Ga_2O_3 to the photocatalytic oxidation of methane. In the case of the $C^{18}O$ molecule, the wavenumber of the C–^{18}O stretching mode shifts to lower wavenumbers (~50 cm^{-1}) compared to that of the non-labelled $C^{16}O$ molecule[34].

Basic characterization of photocatalyst samples. The presence of Pt and Pd for Pt/Ga_2O_3 and Pd/Ga_2O_3 photocatalysts, respectively, was observed by energy dispersive X-ray (EDX) spectroscopy (SU6600; Hitachi). The optical properties of Pt/Ga_2O_3 and Pd/Ga_2O_3 were measured using UV-Vis absorption spectroscopy (V-670; JASCO). The UV-Vis spectra were measured in the diffuse reflectance mode with an integrated sphere. Barium sulfate was used as a reference for the relative reflectance. The crystal structures of the Pt/Ga_2O_3 and Pd/Ga_2O_3 samples were measured using X-ray diffraction (XRD, XRD-6000; Shimadzu). The amount of adsorbed N_2 was measured at 77 K using a Monosorb MS-21 instrument (Quantachrome). The specific surface areas were calculated based on the Brunauer–Emmett–Teller (BET) theory. We also measured the methane adsorption isotherm of Pt/Ga_2O_3 at 77 K using a BELSORP-max instrument (MicrotracBEL). These characterization results are described in Supplementary Section 5.

References

1. Olivos-Suarez, A.I. et al. Strategies for the direct catalytic valorization of methane using heterogeneous catalysis: Challenges and opportunities. *ACS Catal.* **6**, 2965–2981 (2016).
2. Yuliati, L. & Yoshida, H. Photocatalytic conversion of methane. *Chem. Soc. Rev.* **37**, 1592–1602 (2008).
3. Li, Q., Ouyang, Y., Li, H., Wang, L. & Zeng, J. Photocatalytic conversion of methane: Recent advancements and prospects. *Angew. Chem. Int. Ed.* **61**, e202108069 (2022).
4. Song, H., Meng, X., Wang, Z.-J., Liu, H. & Ye, J. Solar-energy-mediated methane conversion. *Joule* **3**, 1606–1636 (2019).
5. Villa, K. & Galan-Mascaros, J.R. Nanostructured photocatalysts for the production of methanol from methane and water. *ChemSusChem* **14**, 2023–2033 (2021).
6. Xie, J. et al. Highly selective oxidation of methane to methanol at ambient conditions by titanium dioxide-supported iron species. *Nat. Catal.* **1**, 889–896 (2018).
7. Zhou, Y., Zhang, L. & Wang, W. Direct functionalization of methane into ethanol over copper modified polymeric carbon nitride via photocatalysis. *Nat. Commun.* **10**, 506 (2019).
8. Wang, Y. et al. Mimicking natural photosynthesis: Solar to renewable H_2 fuel synthesis by Z-scheme water splitting systems. *Chem. Rev.* **118**, 5201–5241 (2018).
9. Xu, C., Ravi Anusuyadevi, P., Aymonier, C., Luque, R. & Marre, S. Nanostructured materials for photocatalysis.

Chem. Soc. Rev. **48**, 3868–3902 (2019).

10. Luo, S., Ren, X., Lin, H., Song, H. & Ye, J. Plasmonic photothermal catalysis for solar-to-fuel conversion: Current status and prospects. *Chem. Sci.* **12**, 5701–5719 (2021).
11. Zhou, X. & Dong, H. A theoretical perspective on charge separation and transfer in metal oxide photocatalysts for water splitting. *ChemCatChem* **11**, 3688–3715 (2019).
12. Takata, T. et al. Photocatalytic water splitting with a quantum efficiency of almost unity. *Nature* **581**, 411–414 (2020).
13. Tsao, C.-W., Fang, M.-J. & Hsu, Y.-J. Modulation of interfacial charge dynamics of semiconductor heterostructures for advanced photocatalytic applications. *Coord. Chem. Rev.* **438**, 213876 (2021).
14. Linsebigler, A.L., Lu, G. & Yates, J.T. Photocatalysis on TiO_2 surfaces: Principles, mechanisms, and selected results. *Chem. Rev.* **95**, 735–758 (1995).
15. Kudo, A. & Miseki, Y. Heterogeneous photocatalyst materials for water splitting. *Chem. Soc. Rev.* **38**, 253–278 (2009).
16. Li, X., Yu, J., Jaroniec, M. & Chen, X. Cocatalysts for selective photoreduction of CO_2 into solar fuels. *Chem. Rev.* **119**, 3962–4179 (2019).
17. Meng, A., Zhang, L., Cheng, B. & Yu, J. Dual cocatalysts in TiO_2 photocatalysis. *Adv. Mater.* **31**, 1807660 (2019).
18. Wang, Q. & Domen, K. Particulate photocatalysts for light-driven water splitting: Mechanisms, challenges, and design strategies. *Chem. Rev.* **120**, 919–985 (2020).
19. Amano, F., Akamoto, C., Ishimaru, M., Inagaki, S. & Yoshida, H. Pressure-induced dehydrogenative coupling of methane to ethane by platinum-loaded gallium oxide photocatalyst. *Chem. Commun.* **56**, 6348–6351 (2020).
20. Sato, H. et al. Critical impacts of interfacial water on the photocatalytic C–H conversion of methane. Preprint at https://doi.org/10.26434/chemrxiv-2022-lcgwv (2022).
21. Shirai, K. et al. Effect of water adsorption on carrier trapping dynamics at the surface of anatase TiO_2 nanoparticles. *Nano Lett.* **16**, 1323–1327 (2016).
22. Sarwana, W., Anzai, A., Takami, D., Yamamoto, A. & Yoshida, H. Carbon monoxide as an intermediate product in the photocatalytic steam reforming of methane with lanthanum-doped sodium tantalate. *Catal. Sci. Technol.* **11**, 5534–5542 (2021).
23. Wei, J. & Iglesia, E. Mechanism and site requirements for activation and chemical conversion of methane on supported Pt clusters and turnover rate comparisons among noble metals. *J. Phys. Chem. B* **108**, 4094–4103 (2004).
24. Tu, W., Ghoussoub, M., Singh, C.V. & Chin, Y.C. Consequences of surface oxophilicity of Ni, Ni-Co, and Co clusters on methane activation. *J. Am. Chem. Soc.* **139**, 6928–6945 (2017).
25. Bagotzky, V.S., Vassiliev, Y.B. & Khazova, O.A. Generalized scheme of chemisorption, electrooxidation and electroreduction of simple organic compounds on platinum group metals. *J. Electroanal. Chem.* **81**, 229–238 (1977).
26. Psofogiannakis, G., St-Amant, A. & Ternan, M. Methane oxidation mechanism on Pt(111): A cluster model DFT study. *J. Phys. Chem. B* **110**, 24593–24605 (2006).
27. Yu, L., Shao, Y. & Li, D. Direct combination of hydrogen evolution from water and methane conversion in a

photocatalytic system over Pt/TiO_2. *Appl. Catal. B* **204**, 216–223 (2017).

28. Yoshinobu, J., Ogasawara, H. & Kawai, M. Broken symmetry of adsorbed methane and self-limiting photoinduced dissociation on Pt(111). *Surf. Sci.* **363**, 234–239 (1996).
29. Gutierrez-Gonzalez, A. & Beck, R.D. Quantum state and surface-site-resolved studies of methane chemisorption by vibrational spectroscopies. *Phys. Chem. Chem. Phys.* **22**, 17448–17459 (2020).
30. Panayotov, D.A., Burrows, S.P. & Morris, J.R. Photooxidation mechanism of methanol on rutile TiO_2 nanoparticles. *J. Phys. Chem. C* **116**, 6623–6635 (2012).
31. Wolski, L., El-Roz, M., Daturi, M., Nowaczyk, G. & Ziolek, M. Insight into methanol photooxidation over mono- (Au, Cu) and bimetallic (AuCu) catalysts supported on niobium pentoxide — an operando-IR study. *Appl. Catal. B* **258**, 117978 (2019).
32. Aleksandrov, H.A., Neyman, K.M., Hadjiivanov, K.I. & Vayssilov, G.N. Can the state of platinum species be unambiguously determined by the stretching frequency of an adsorbed CO probe molecule? *Phys. Chem. Chem. Phys.* **18**, 22108–22121 (2016).
33. Avanesian, T. et al. Quantitative and atomic-scale view of CO-induced Pt nanoparticle surface reconstruction at saturation coverage via DFT calculations coupled with in situ TEM and IR. *J. Am. Chem. Soc.* **139**, 4551–4558 (2017).
34. Richard, M., Duprez, D., Bion, N. & Can, F. Investigation of methane oxidation reactions over a dual-bed catalyst system using ^{18}O labelled DRIFTS coupling. *ChemSusChem* **10**, 210–219 (2017).
35. Kuhn, W.K., Szanyi, J. & Goodman, D.W. CO adsorption on Pd(111): The effects of temperature and pressure. *Surf. Sci.* **274**, L611–L618 (1992).
36. Migani, A. & Blancafort, L. What controls photocatalytic water oxidation on rutile TiO_2(110) under ultra-high-vacuum conditions? *J. Am. Chem. Soc.* **139**, 11845–11856 (2017).
37. Litke, A. et al. Role of adsorbed water on charge carrier dynamics in photoexcited TiO_2. *J. Phys. Chem. C* **121**, 7514–7524 (2017).
38. Shirai, K. et al. Water-assisted hole trapping at the highly curved surface of nano- TiO_2 photocatalyst. *J. Am. Chem. Soc.* **140**, 1415–1422 (2018).
39. Tachikawa, T., Yonezawa, T. & Majima, T. Super-resolution mapping of reactive sites on titania-based nanoparticles with water-soluble fluorogenic probes. *ACS Nano* **7**, 263–275 (2013).
40. Yamakata, A. et al. Behavior and energy states of photogenerated charge carriers on Pt- or CoO_x-loaded $LaTiO_2N$ photocatalysts: Time-resolved visible to mid-infrared absorption study. *J. Phys. Chem. C* **118**, 23897–23906 (2014).
41. Wang, D., Liu, Z.-P. & Yang, W.-M. Revealing the size effect of platinum cocatalyst for photocatalytic hydrogen evolution on TiO_2 support: A DFT study. *ACS Catal.* **8**, 7270–7278 (2018).
42. Li, X., Xie, J., Rao, H., Wang, C. & Tang, J. Platinum- and CuO_x-decorated TiO_2 photocatalyst for oxidative coupling of methane to C_2 hydrocarbons in a flow reactor. *Angew. Chem. Int. Ed.* **59**, 19702–19707 (2020).
43. Zhang, W. et al. High-performance photocatalytic nonoxidative conversion of methane to ethane and hydrogen by heteroatoms-engineered TiO_2. *Nat. Commun.* **13**, 2806 (2022).

44. Muhich, C.L., Zhou, Y., Holder, A.M., Weimer, A.W. & Musgrave, C.B. Effect of surface deposited Pt on the photoactivity of TiO_2. *J. Phys. Chem. C* **116**, 10138–10149 (2012).

45. Yoshida, M. et al. ATR-SEIRAS investigation of the Fermi level of Pt cocatalyst on a gan photocatalyst for hydrogen evolution under irradiation. *J. Am. Chem. Soc.* **131**, 13218–13219 (2009).

46. Kokawa, R., Ohta, M., Sasahara, A. & Onishi, H. Kelvin probe force microscopy study of a Pt/TiO_2 catalyst model placed in an atmospheric pressure of N_2 environment. *Chem. Asian J.* **7**, 1251–1255 (2012).

47. Zhou, P. et al. Modulating the photocatalytic redox preferences between anatase TiO_2 {001} and {101} surfaces. *Chem. Commun.* **53**, 787–790 (2017).

48. Singh, S.P., Anzai, A., Kawaharasaki, S., Yamamoto, A. & Yoshida, H. Non-oxidative coupling of methane over Pd-loaded gallium oxide photocatalysts in a flow reactor. *Catal. Today* **375**, 264–272 (2021).

49. Tyagi, A., Matsumoto, T., Yamamoto, A., Kato, T. & Yoshida, H. Metal cocatalyst directing photocatalytic acetonylation of toluene via dehydrogenative cross-coupling with acetone. *Catal. Lett*. **150**, 31–38 (2020).

50. Mori, S. & Saito, S. C(sp^3)–H functionalization with styrenes via hydrogen-atom transfer to an aqueous hydroxyl radical under photocatalysis. *Green Chem*. **23**, 3575–3580 (2021).

51. Yamauchi, M., Saito, H., Sugimoto, T., Mori, S. & Saito, S. Sustainable organic synthesis promoted on titanium dioxide using coordinated water and renewable energies/resources. *Coord. Chem. Rev*. **472**, 214773 (2022).

52. Lin, C.-H., Chao, J.-H., Liu, C.-H., Chang, J.-C. & Wang, F.-C. Effect of calcination temperature on the structure of a Pt/TiO_2 (B) nanofiber and its photocatalytic activity in generating H_2. *Langmuir* **24**, 9907–9915 (2008).

53. Zhou, R., Zhao, B. & Yue, B. Effects of CeO_2-ZrO_2 present in Pd/Al_2O_3 catalysts on the redox behavior of PdO_x and their combustion activity. *Appl. Surf. Sci.* **254**, 4701–4707 (2008).

Acknowledgments

This work was supported by JST-PRESTO [No. JPMJPR16S7]; JSPS KAKENHI Grant-in-Aid for Specially Promoted Research [No. JP17H06087], Grant-in-Aid for JSPS Fellows [No. JP22J01398], Grant-in-Aid for Scientific Research (A) [No. JP19H00865, JP22H00296]; Joint Research by the National Institutes of Natural Sciences (NINS) [No. 01112104]; Special Project by Institute for Molecular Science [22IMS1101]. The authors acknowledge Dr. Koutaro Takeyasu, Akira Yamamoto, Hisao Yoshida, Fumiaki Kato, Norihiro Aiga, Kazuya Watanabe, Yoshiyasu Matsumoto, Susumu Saito, Shogo Mori, Fumiaki Amano and Atsunori Sakurai for fruitful discussion and/or contribution at an early stage in this research.

Author contributions

T.S. supervised and conceived the overall investigation. H.S., H.S., and T.H. prepared the photocatalysts and performed the characterizations, photocatalytic activity tests, and spectroscopic measurements. All the authors discussed the results and gave comments on the manuscript. H.S. and T.S. wrote the manuscript.

Competing interests

The authors declare no competing financial interest.

Additional information

Correspondence and requests for materials should be addressed to T.S.